Rare Metal Materials and Engineering
Volume 50, Issue 5, May 2021
Available online at www.rmme.ac.cn

Science Press

Cite this article as: Li Rui, Chen Xuan, Wang Juan, et al. Characterization and Oxidation Resistance of Multilayered Silicide Coating on Bimodal Mo-Si-B Substrate[J]. Rare Metal Materials and Engineering, 2021, 50(05): 1531-1541.

ARTICLE

Characterization and Oxidation Resistance of Multilayered Silicide Coating on Bimodal Mo-Si-B Substrate

Li Rui, Chen Xuan, Wang Juan, Li Bin, Wang Tao, Yan Fuxue, Zhang Guojun

School of Materials Science and Engineering, Xi'an University of Technology, Xi'an 710048, China

Abstract: To enhance the surface protection of the bimodal Mo-Si-B alloy and simultaneously maintain its superior mechanical properties, a multilayered coating ($MoSi_2$, Mo_5Si_3 and Mo_5SiB_2/MoB) was synthesized on its surface via pack cementation. Results show that, compared to the coating on the fine-grained substrate, the coating surface on the bimodal substrate is rougher and exhibits bimodal microstructure. Additionally, the fracture toughness of bimodal alloy after coating is acceptable. The distributed La_2O_3 particles toughen the coating. Besides, the coated bimodal specimens show excellent oxidation resistance at 1100~1300 °C, which is attributed to the quick formation of a thin and self-healing SiO_2-B_2O_3 film on the coating surface. With increasing the temperature, the thickness of SiO_2-B_2O_3 film and the oxidation product Mo_5Si_3 increase because the viscosity of SiO_2-B_2O_3 film decreases. Also, improving temperature promotes the interdiffusion of Si and B, accelerating the growth of Mo_5Si_3 and Mo_5SiB_2/MoB layers. Compared to the coated bimodal alloy, the coated fine-grained alloy exhibits more oxidation mass gain at 1300 °C since the unimodal $MoSi_2$ coating has more grain boundaries.

Key words: $MoSi_2$ coating; Mo-12Si-8.5B alloy; bimodal α-Mo grains; pack cementation; oxidation resistance

In recent decades, improving the energy efficiency of gas turbine systems at higher temperatures in the fields of aerospace and power generation industry is paid more and more attention[1,2]. Mo-Si-B alloys in the ternary phase field of α-Mo-Mo_3Si-Mo_5SiB_2 are potential candidates for high-temperature structural applications because they have high melting points, superior high-temperature (creep) strength and good high-temperature oxidation resistance[3,4]. Particularly, obtaining a fine-grained (FG) microstructure for Mo-Si-B alloys can further improve the oxidation resistance[5,6]. However, the poor ductility and fracture toughness (~9 MPa·$m^{1/2}$) at room temperature is a crucial drawback restricting the extensive applications of FG Mo-Si-B because of the restricted dislocation storage capability in the fine grains[7,8].

For many metal materials with nanocrystalline (NC) or ultrafine grains (UFGs), developing a microstructure with bimodal grain size distribution (micron-sized coarse grains distributed in a NC and UFG matrix) can improve the ductility of materials without much loss of their strength[9]. The coarse grain (CG) contributes to the high ductility whereas the UFG provides high strength. Previous study confirmed that some kinds of FG Mo-12Si-8.5B-0.57wt% La_2O_3 alloys with bimodal FG/CG α-Mo grains were fabricated by powder metallurgy[10]. A significantly enhanced fracture toughness (11.3~12.5 MPa·$m^{1/2}$) was achieved without much decrease of compression strength.

Possessing a superior high-temperature oxidation resistance is also crucial to the bimodal Mo-Si-B alloy. At 1000~1300 °C, the α-Mo phase quickly oxidizes to volatile MoO_3 in the initial stage[11]. Meanwhile, an in-situ SiO_2-B_2O_3 passive layer forms by the oxidation of Mo_3Si and Mo_5SiB_2 phases. When the continuous SiO_2-B_2O_3 layer flows and seals the alloy surface, the steady-state oxidation begins[12]. Actually, for the bimodal microstructure, the large size and dispersive distribution of CG α-Mo regions increase the diffusion distance of boron and silicon elements and inhibit the flowing and coverage of SiO_2-

Received date: December 07, 2020
Foundation item: National Natural Science Foundation of China (51674196, 51601144, 51701162); National Key Research and Development Program of China (2017YFB0702403); Innovative Talents Promotion Plan of Shaanxi (2019KJXX-071); Excellent Doctoral Innovation Fund of Xi'an University of Technology (310-252071705)
Corresponding author: Zhang Guojun, Ph. D., Professor, School of Materials Science and Engineering, Xi'an University of Technology, Xi'an 710048, P. R. China, Tel: 0086-29-82312592, E-mail: zhangguojun@mail.xjtu.edu.cn

B_2O_3 scale, which has a bad effect on the oxidation behavior at the initial stage and even the subsequent stage.

To enhance the surface oxidation resistance of refractory metal-based materials, a $MoSi_2$ coating was synthesized on the metal surface due to outstanding oxidation resistance of $MoSi_2$ at 1700 °C[13-15]. The halide activated pack cementation (HAPC) technique is an effective fabrication method. The advantage of this technique is that it is easy to operate and control the thickness of desired coating as well as achieve the metallurgical bond between the substrate and coating. Wang et al[16] synthesized a single $MoSi_2$ coating and a $MoSi_2$/MoB composite coating on Mo-based alloy by HAPC. Majumdar[17] and Tang[18] et al reported that the HAPC can successfully deposit $MoSi_2$ onto a Mo-9Si-8B-0.75Y alloy and a Mo-12Si-8B alloy, separately, which improves the surface oxidation resistance of alloys at 750~1400 °C.

When a $MoSi_2$ matrix coating is attempted to fabricate on the bimodal Mo-Si-B alloy to improve the oxidation resistance of alloy surface, the superior mechanical properties of substrate are expected to be retained. Li et al[8] found that the microstructure and mechanical properties of Mo-12Si-8.5B-3Zr alloy hardly change after annealing at 1600 °C for 3 h. Thus, the designed deposition temperature should be below 1600 °C. Besides, the formation of $MoSi_2$ coating originates from the reaction between the active Si atoms and substrate phases, as well as the interdiffusion of active elements. When the Si atom reacts with the CG α-Mo regions, the reaction rate in the CG α-Mo regions is different from that in the surrounding FG three-phase regions.

In this work, a multilayered silicide coating was prepared on a bimodal Mo-12Si-8.5B-0.57wt% La_2O_3 alloy after hot pressing (HP) using HAPC technique at 1200 °C. To investigate the microstructural difference of coatings on the bimodal and unimodal substrates, an as-HPed FG Mo-12Si-8.5B-0.57wt% La_2O_3 alloy was pack cemented by the same coating process. The effect of La_2O_3 particles on the coating was discussed. Besides, the isothermal oxidation behavior of the uncoated bimodal alloys as well as the coated bimodal and FG alloys at 1100~1300 °C was analyzed. The microstructure evolution, oxidized scale structures and oxidation resistance mechanisms of coating at different temperatures were explored.

1 Experiment

A FG Mo-12Si-8.5B-0.57wt% La_2O_3 alloy with a bimodal α-Mo grains was fabricated by three kinds of original powders, involving Mo-0.6wt% La_2O_3 (≤6.5 μm)[19], Si (99.99wt%, ≤5.0 μm), and B (99.95wt%, ≤1.0 μm). This alloy was prepared through blended powders of ball milled Mo-Si-B-La_2O_3 powders and non-milled Mo-La_2O_3 powders with the mass ratio of 80:20 via hot pressing sintering. For comparative study, an FG Mo-12Si-8.5B-0.57wt% La_2O_3 alloy was prepared by the mixture of Mo-0.6wt% La_2O_3, Si, and B powders via one-step high energy ball milling (HEBM), followed by the same HP sintering process. The detailed preparation methods of these two alloys were presented earlier[10]. HP process was conducted at 1600 °C for 3 h with a pressure of 49 MPa.

Microstructure of as-HPed alloys was characterized by an electron back scatter diffraction (EBSD) with step sizes of 0.4 μm using a ZEISS MERLIN compact scanning electron microscopy (SEM). Alloy microstructure was further determined by transmission electron microscopy (TEM, JEM-2100Plus).

The HAPC process was employed to produce a silicide coating through vapor-phase depositing on the as-HPed bimodal and FG samples. A powder mixture composed of 20wt% Si (99.99% purity, ≤5 μm), 5wt% NH_4Cl activator (50~100 μm) and 75wt% Al_2O_3 filler (≤50 μm) was prepared. The packs were prepared by filling the powder mixture around the alloy substrate in a cylindrical alumina crucible. Subsequently, the crucible was inserted into a horizontal tube furnace. Finally, the deposition process was conducted at 1200 °C for 5 h in a flowing argon atmosphere.

Room temperature fracture toughness was examined by three-point bending tests by single-edge notch bend specimens. The dimensions of specimens were 3 mm×4 mm×26 mm with a notch of 0.25 mm in width and 2 mm in depth. The bending tests were carried out under a loading speed of 0.05 mm/min using a universal material testing machine. SEM was used to observe the fracture surfaces.

Isothermal oxidation tests were performed in a perpendicular tube furnace in the static laboratory air at 1100, 1200 and 1300 °C for 30 h. The dimensions of specimens were Φ15 mm×4 mm. The oxidation kinetics of samples were analyzed using a continuous thermogravimetric analysis (TGA) system.

The roughness of coatings surface was analyzed using a 3D laser scanning confocal microscope (LEXT OLS4000). The surface and cross-sectional microstructures of coating and oxidation of samples were analyzed using SEM equipped with back-scattered-electron (BSE) imaging and energy dispersive spectroscopy (EDS).

2 Results

2.1 Microstructure of as-HPed bimodal and unimodal alloys

The EBSD images of as-HPed (bimodal) and FG (unimodal) Mo-Si-B alloys are shown in Fig.1a and 1b, respectively[10]. The red, yellow and olive phases are α-Mo, Mo_3Si and Mo_5SiB_2, respectively. In Fig.1a, the bimodal alloy presents an interpenetrating microstructure (mixture of three phases). The α-Mo grains exhibit a bimodal FG/CG structure whereas the Mo_3Si/Mo_5SiB_2 grains show a unimodal FG structure. In Fig. 1b, the unimodal alloy shows that the submicron-scaled FG Mo_3Si/Mo_5SiB_2 particles are distributed dispersedly in submicron-scaled FG α-Mo matrix. The area fraction distributions of α-Mo, Mo_3Si and Mo_5SiB_2 grains of as-HPed bimodal and FG alloys are presented in Fig.1c and 1d, respectively[10]. In Fig.1c, the α-Mo, Mo_3Si and Mo_5SiB_2 grains with their size below 2 μm constitute the FG regions. Other α-Mo grains with their size above 2 μm form the CG regions. The average grain sizes of FG α-Mo, CG α-Mo, Mo_3Si and Mo_5SiB_2 are 0.63, 3.07, 0.55 and 0.51 μm, respectively. In the FG alloy, the average grain sizes of α-Mo, Mo_3Si and Mo_5SiB_2 are 0.55, 0.48

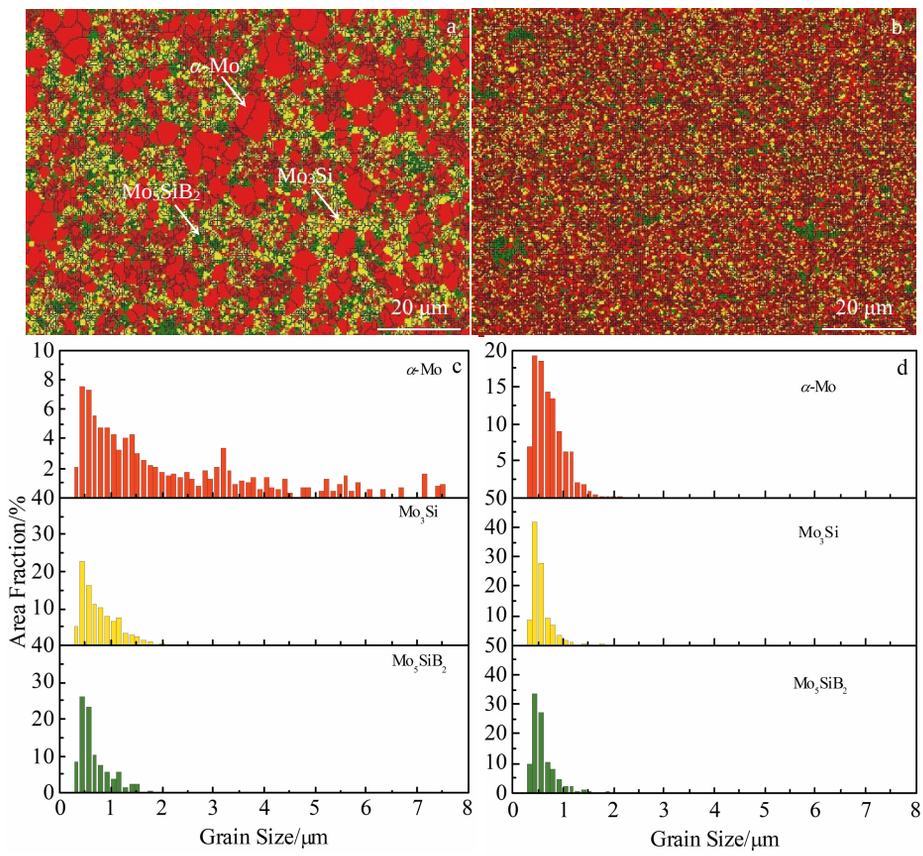

Fig.1 EBSD images (a, b) and area fraction distributions (c, d) of the as-HPed bimodal (a, c) and FG (b, d) alloys[10]

and 0.49 μm, respectively (Fig.1d).

Fig.2 is the TEM images of as-HPed bimodal alloy including the CG regions (Fig.2a) and FG regions (Fig.2b). Fig.2a presents a coarse α-Mo grain (~2.05 μm) distributed in the FG regions. Fig.2b shows that the grain size of α-Mo and intermetallic in the FG regions is at submicron scale. Fig.2c shows the nanoscale La_2O_3 particle distributed at the grain boundary of α-Mo and Mo_3Si. The high resolution transmission electron microscopy (HRTEM) image (Fig. 2d) further shows that the measured interplanar space of La_2O_3 (110), Mo (001) and Mo_3Si (211) planes is 0.309, 0.312 and 0.202 nm, respectively.

2.2 Microstructure of silicide coating

Typical surfaces of the silicide coatings form on the as-HPed bimodal and FG samples after pack cementation, as shown in Fig.3a and 3b, respectively. EDS analysis confirms that the outer coating is mainly $MoSi_2$. The high-magnified image (inset in Fig.3a) shows that the surface exhibits the bimodal microstructure. Some large-sized humps (7.5~13.5 μm) are distributed randomly among the fine humps (2.6~3.5 μm). In Fig.3b, the fine humps are distributed dispersedly on the surface, without coarse humps.

The surface roughness of the $MoSi_2$ coatings on the bimodal and FG substrates is shown in Fig.4a and 4b, respectively. The roughness space arithmetic mean height (RS_a) values of the $MoSi_2$ coatings on the bimodal and FG substrates are 0.595 and 0.437 μm, respectively, which indicates that the $MoSi_2$ coating on the bimodal substrate is rougher than that on the FG substrate.

The cross-sectional image of coated bimodal sample displays the formation of three coating layers on the substrate (Fig.5a). The outermost layer is mainly $MoSi_2$ (~25.5 μm) and the middle layer is Mo_5Si_3 (~3.2 μm). EDS results confirm that the La_2O_3 particles are distributed in the $MoSi_2$ and Mo_5Si_3 layers (Fig.5b and 5c). Fig.5d exhibits a mixed coating area of Mo_5SiB_2/MoB (~2.1 μm) forming between the Mo_5Si_3 layer and substrate. The La_2O_3 particles are distributed in the Mo_5SiB_2/MoB layer (Fig.5e). Fig.5f is the cross-sectional image of coated FG sample. The coating structure of coated FG sample is similar to that of coated bimodal sample. Every coating layer on the FG substrate is flatter and more uniform than that on the bimodal substrate.

During the cementation process of Si pack, $SiCl_x$ vapor produces from the activator NH_4Cl reacting with Si powders at high temperature. Subsequently, the $SiCl_x$ vapor is dissociated on the active alloy surface releasing Si in atomistic form[20]. During the coating process, an obvious chemical potential gradient of Si at the interface of vapor and substrate generates a flux of Si into the substrate, which causes the growth of $MoSi_2$ coating[21]. The chemical reactions contributing to the growth of $MoSi_2$ are shown as follows:

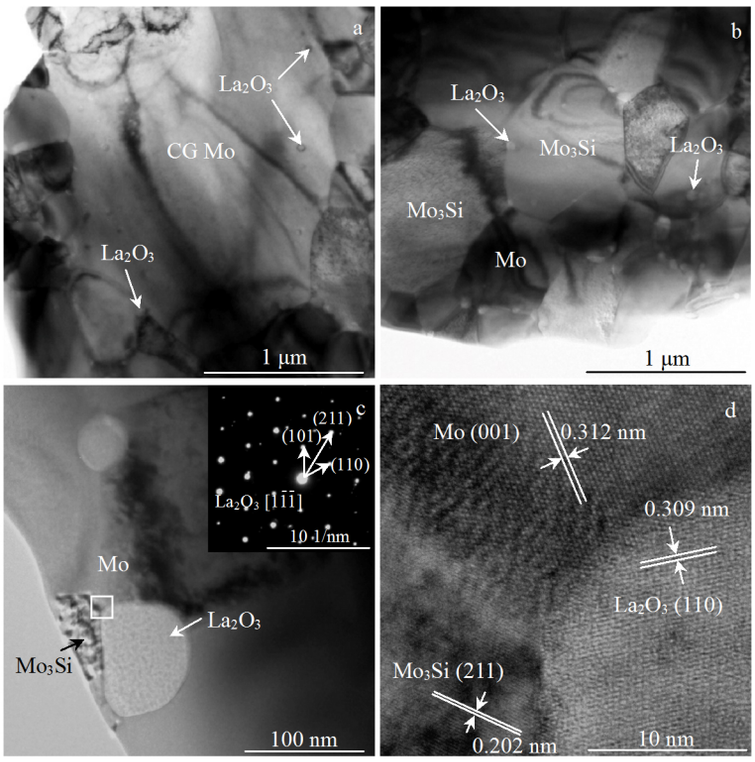

Fig.2 Microstructures of CG (a) and FG (b) regions; La_2O_3 particles distributed at the grain boundary of α-Mo and Mo_3Si (c); HRTEM image of the square area in Fig.2c (d)

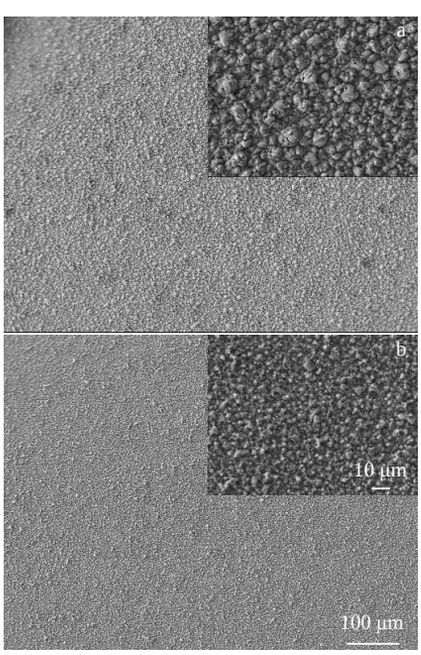

Fig.3 SEM images of coated bimodal (a) and coated FG (b) sample surfaces

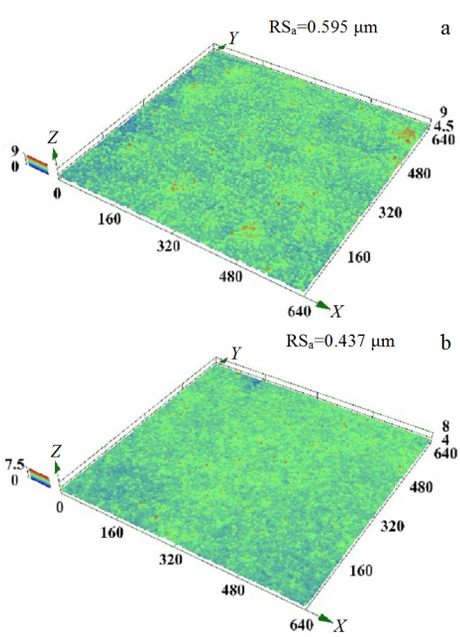

Fig.4 Surface roughness of the $MoSi_2$ coatings on bimodal (a) and FG (b) substrates

$$Mo+2Si \rightarrow MoSi_2 \quad (1)$$

$$Mo_3Si+5Si \rightarrow 3MoSi_2 \quad (2)$$

$$Mo_5SiB_2+5Si \rightarrow 3MoSi_2+2MoB \quad (3)$$

It can be speculated that there are very fine MoB particles

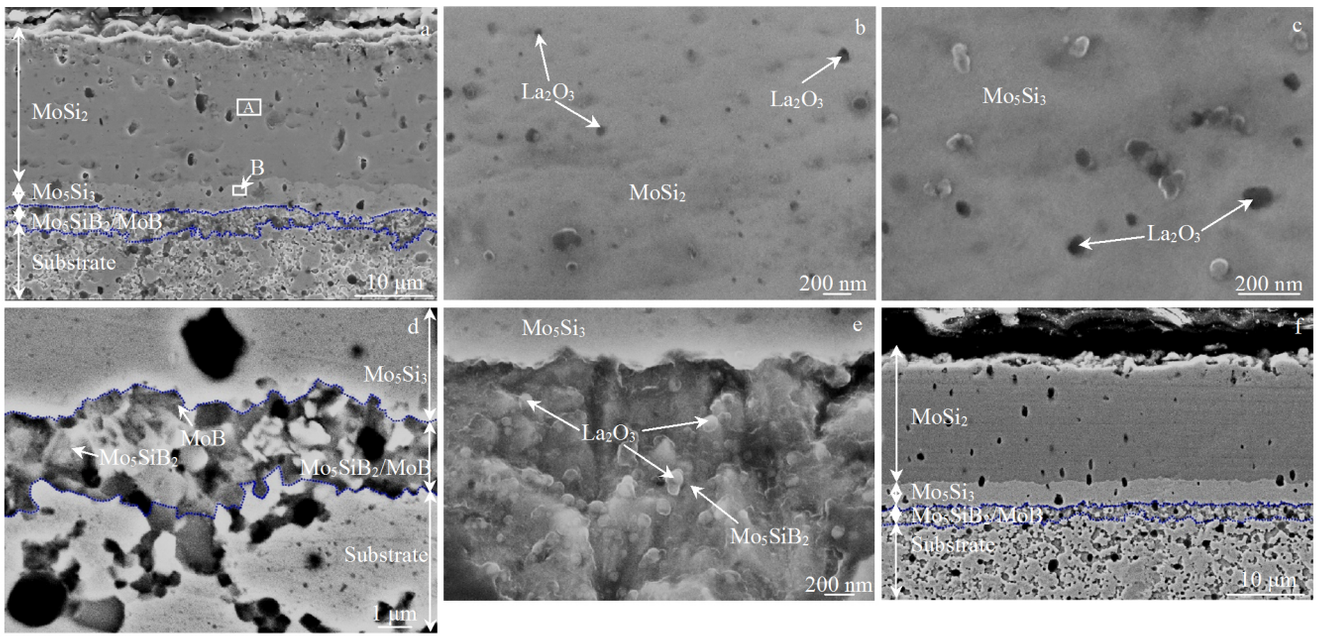

Fig.5 BSE images of cross-sectional morphologies of coated bimodal sample (a~c): (a) panorama, (b) area A in Fig.5a, and (c) area B in Fig.5a; SEM images of cross-sectional morphologies of Mo_5SiB_2/MoB layer (d, e); BSE image of cross-sectional morphology of coated FG sample (f)

distributed in $MoSi_2$ layer (Eq.(3))[17,21]. Fig.6 presents the reaction diffusion pathway between $MoSi_2$ and the substrate composition during the pack cementation. After the formation of an initial outer $MoSi_2$ coating, the finite diffusion source of Si from the $MoSi_2$ coating results in a transient diffusion path. The Mo_5Si_3 and Mo_5SiB_2/MoB form sequentially, and meanwhile the $MoSi_2$ layer is consumed. The Mo_5Si_3 layer remains at a local equilibrium with the Mo_5SiB_2 and MoB phases. With the continued pack treatment, the Si source is supplemented continuously, resulting in the continuous development of three coating layers.

The growth behavior of $MoSi_2$-matrix coatings on the Mo-Si-B substrate can be explained by the thermodynamic and kinetic analysis. The Gibbs free energy change (ΔG) of Eq.(1~3) at different temperatures is shown in Fig. 7. Majumdar et al[22] established a theoretical model equation correlating the silicide coating growth on Mo-based alloy substrate with pack composition and processing conditions. Thus, the kinetic equation for the silicide coating growth process on the bimodal alloy can be represented as follows[22]:

$$h = \frac{k_0}{T^{1/2}} W_{Si}^{1/2} W_{NH_4Cl} t^{1/2} \exp\left(-\frac{E_a}{RT}\right) \quad (4)$$

where h is the silicide coating thickness; k_0 is a constant; W_{Si} and W_{NH_4Cl} are the mass fractions of Si and NH_4Cl activator in the packs, respectively; E_a is the activation energy for the coating growth process; R is the equilibrium gas constant. Thus, the change of coating thickness relates to W_{Si}, W_{NH_4Cl}, deposition temperature (T) and time (t). When the pack composition and processing conditions are constant, the reactions in Eq.(2)

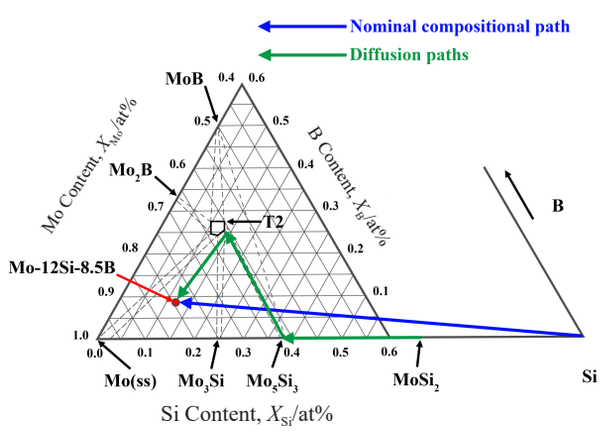

Fig.6 Schematic diagram of reaction diffusion paths of Si element in Mo-12Si-8.5B alloy via pack cementation

and Eq.(3) occur easily, and the reaction rate of reactions in Eq.(2) and Eq.(3) are higher than that of reaction in Eq.(1), because reactions in Eq.(2) and Eq.(3) have more negative ΔG, and Mo_3Si and Mo_5SiB_2 can supply additional Si to synthesize $MoSi_2$ coating. When Si reacts with the CG α-Mo regions in the bimodal substrate, the reaction rate in the CG α-Mo regions becomes lower than that in the surrounding FG three-phase regions. Besides, the number of grain boundaries is less in the CG α-Mo regions, decreasing the barriers of Si diffusion. The CG α-Mo regions are easy to form the coarse $MoSi_2$, and even coarse Mo_5Si_3 and Mo_5SiB_2/MoB phases. So the bi-

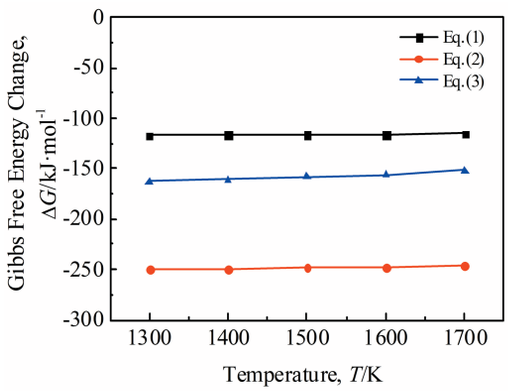

Fig.7 Gibbs free energy change (ΔG) of reactions in Eq.(1~3) at different temperatures

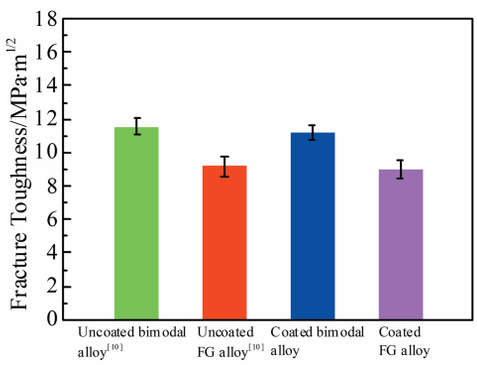

Fig.8 Fracture toughness of uncoated and coated alloys

modal $MoSi_2$ phase appears on the coating surface. The interfaces in the coating layers on the bimodal substrate are not flat compared to those on the unimodal substrate. During the reaction diffusion, the La_2O_3 particles distributed in the coating impede the grain boundary migration of silicide to some extent, avoiding the excessive growth of grains[23].

2.3 Evaluation of mechanical properties

Fig. 8 shows the fracture toughness of bimodal and FG alloys before and after coating. After coating, the fracture toughness of bimodal and FG alloys barely changes. Fig.9a presents the fracture surface of coated bimodal alloy after bending tests. The microstructure of $MoSi_2$ layer is columnar. In Fig.9b, the fracture surface of $MoSi_2$ layer exhibits intragranular and intergranular fractures. The La_2O_3 particles are distributed at the grain boundaries and in the grain interiors of $MoSi_2$. Fig.9c shows that some microcracks form around the intragranular La_2O_3 particles in the $MoSi_2$ layer. Fig. 9d exhibits that the microstructure of the Mo_5Si_3 layer is equiaxial and the Mo_5Si_3 shows intragranular and intergranular fractures. Some residual holes distributed in the transgranular facets of the $MoSi_2$ and Mo_5Si_3 grains are produced by the extraction of La_2O_3 particles. Fig. 9e presents that the fracture surface of coated FG alloy is flat. Most grains in the Mo_5Si_3 and Mo_5SiB_2/MoB layers show intragranular fracture (Fig.9f).

Because the silicide coating is very thin, the difference of coating interfaces on the bimodal and FG alloys has little impact on the fracture toughness of alloys. During the fracture process of coated bimodal alloy, the cracks in the substrate are blunted and deflected by the CG α-Mo regions, resulting in the direction change of crack propagation and the microcracks production[10]. Thus, the fracture surface of bimodal substrate

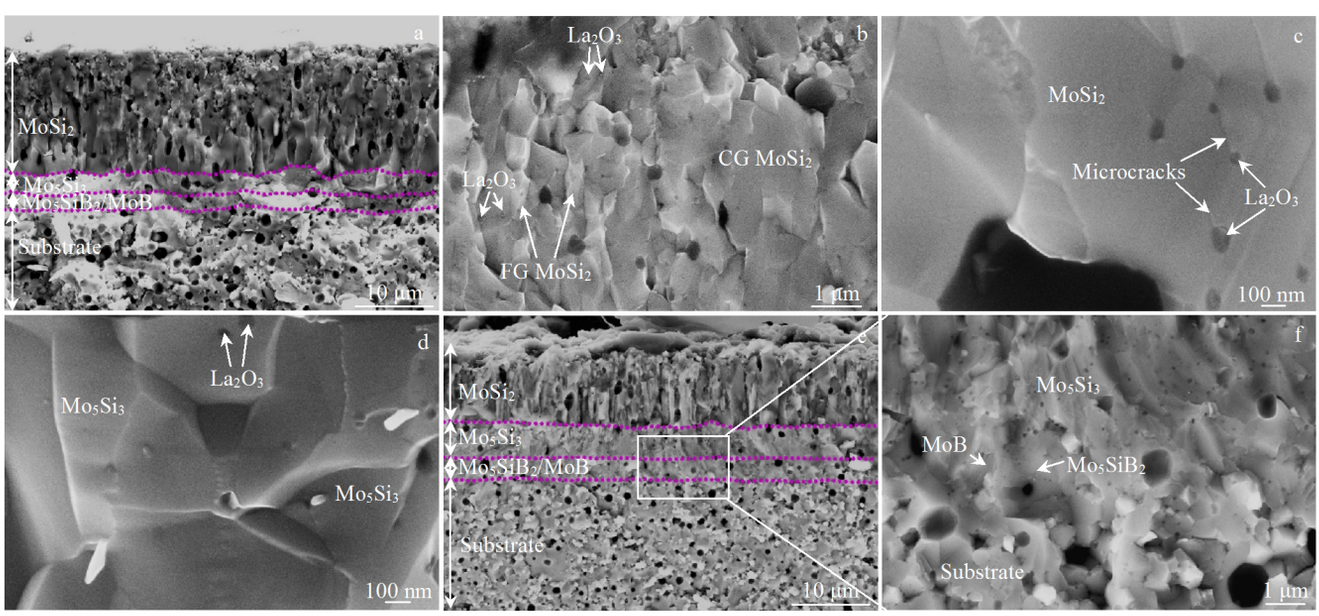

Fig.9 SEM images of fracture surfaces of coated bimodal (a~d) and FG (e, f) alloys after bending testing

is craggy. Subsequently, these cracks extend towards the coating surface. When some cracks are propagated along the grain boundaries of silicide, the intergranular fracture occurs. Other cracks propagated in the grain interior of silicide induce the intragranular fracture. So the fracture surface of silicide coating is also craggy and exhibits mixed-mode fracture. However, in the coated FG alloy, the cracks barely deflect by the FG substrate and the microcracks are hardly produced[10]. Thus, the fracture surface of FG substrate is flat. Afterwards, the main crack is propagated through the grain interior of silicide coating, which mainly induces the intragranular fracture.

During the fracture process, the stress/strain concentration at $La_2O_3/MoSi_2$ and La_2O_3/Mo_5Si_3 interfaces is easy to trigger interfacial decohesion and produce microcracks, facilitating the silicide grains to cause transgranular fracture. Besides, the intergranular and intragranular cracks deflect by the La_2O_3 particles. The crack propagating path twists and lengthens. In addition, the La_2O_3 particles have excellent adsorbing oxygen characteristic owing to the strong interactions between rare earth elements and oxygen[23]. Although the fracture toughness of $MoSi_2$ and Mo_5Si_3 is 2~3 $MPa·m^{1/2}$ [24,25], the La_2O_3 particles toughens the coating.

2.4 Isothermal oxidation behavior at 1100~1300 °C

Fig. 10a~10c show the isothermal mass change of uncoated and coated alloys oxidized at 1100~1300 °C for 30 h. The uncoated bimodal alloys show a transient mass loss at the initial stage of 0.5~1 h followed by a continuous decrease in mass at 1100~1300 °C. Compared to the uncoated bimodal alloys, the coated bimodal alloy has the excellent oxidation resistance and shows a very small mass loss at the initial stage followed by a slight increase in mass at 1100~1300 °C when it is oxidized for 30 h. After 30 h, the coated bimodal alloys suffer a marginal mass change of −0.45, +0.32 and +0.71 $mg·cm^{-2}$ at 1100, 1200, and 1300 °C, respectively. The oxidation behavior of coated FG alloy is similar to that of coated bimodal alloy at 1300 °C. After 30 h, the coated FG alloy exhibits a slightly increasing mass change of +1.40 $mg·cm^{-2}$.

2.5 Top surface and cross-sectional microstructures of oxidized specimens

SEM images of surface of the coated bimodal samples after oxidation at varying temperatures for 30 h are shown in Fig. 11. EDS results confirm that the outer scale is mainly SiO_2 at different temperatures. At 1100 °C, the SiO_2 surface is rough (Fig. 11a and 11b). With increasing the temperature, the SiO_2 surface becomes smooth and flat (Fig. 11c and 11d).

Fig. 12a~12c show the BSE images of cross-sectional coated bimodal alloys after oxidization at 1100~1300 °C for 30 h. At 1100 °C (Fig. 12a), the outermost SiO_2 film is very thin. Boron element from fine MoB precipitates may accompany the SiO_2 scale in the form of B_2O_3. The subsequent continuous layers are $MoSi_2$, Mo_5Si_3 and Mo_5SiB_2/MoB accordingly. At 1200 (Fig. 12b) and 1300 °C (Fig. 12c), the oxidized scale structure is similar to that at 1100 °C. With increasing the temperature, the oxidation products Mo_5Si_3 forming between the SiO_2-B_2O_3 film and $MoSi_2$ layer increase. In addition, the average thicknesses of different structural layers on the substrate of coated bimodal specimens after oxidation at different temperatures are presented in Fig. 13. Fig. 12d shows the BSE image of cross-sectional coated FG alloy oxidized at 1300 °C for 30 h. The number of oxidation products Mo_5Si_3 of coated FG alloy is larger than that of coated bimodal alloy at 1300 °C.

3 Discussion

Developing a multilayered coating structure ($MoSi_2$, Mo_5Si_3 and Mo_5SiB_2/MoB) on the bimodal Mo-Si-B substrate via Si-pack cementation can significantly improve the oxidation resistance of alloy surface. Compared to the bimodal specimens, the coated bimodal specimens exhibit a slight mass change (Fig. 10).

The Si-rich $MoSi_2$ matrix (containing fine MoB precipitates) in the coating plays a significant role in improving the oxidation resistance. The possible oxidation reactions are presented as follows:

$$2/7MoSi_2+O_2 \rightarrow 2/7MoO_3+4/7SiO_2 \quad (5)$$

$$5/7MoSi_2+O_2 \rightarrow 1/7Mo_5Si_3+SiO_2 \quad (6)$$

$$4/9MoB+O_2 \rightarrow 4/9MoO_3+2/9B_2O_3 \quad (7)$$

The Gibbs free energy change (ΔG) of reactions in Eq. (5) and Eq. (6) at 1100~1300 °C is shown in Table 1. The more negative value of ΔG of reaction in Eq. (6) indicates that the formation of Mo_5Si_3 is thermodynamically more favorable

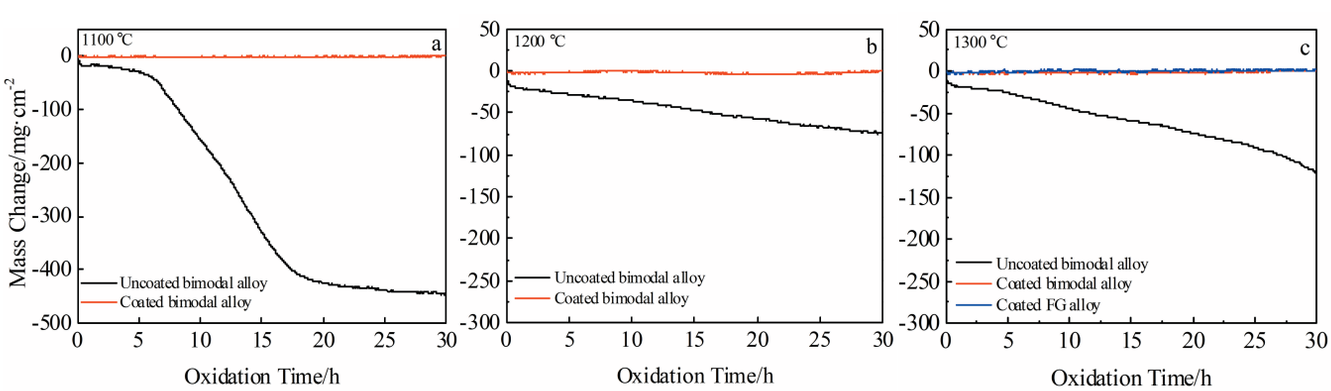

Fig. 10 Isothermal oxidation behavior of uncoated and coated alloys at 1100 °C (a), 1200 °C (b) and 1300 °C (c)

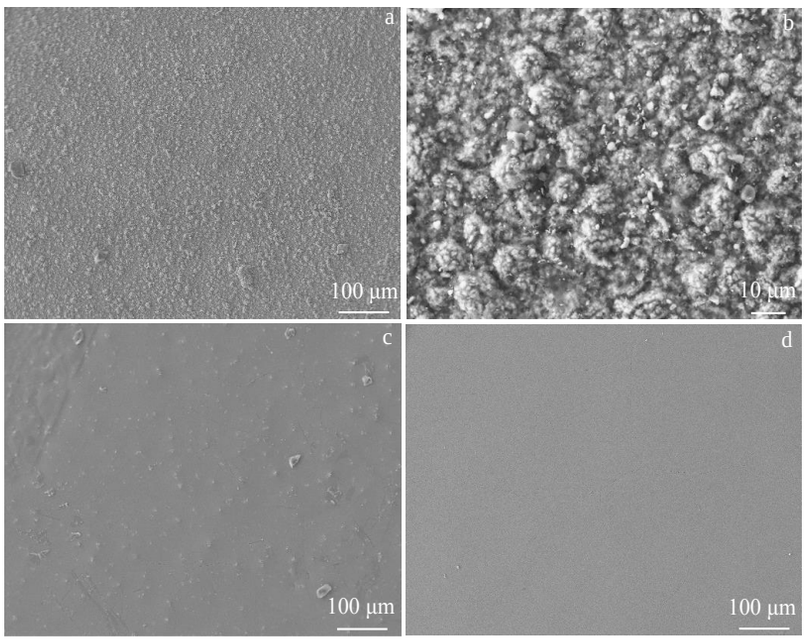

Fig.11 SEM images of surface of coated bimodal samples after oxidation at 1100 °C (a, b), 1200 °C (c) and 1300 °C (d) for 30 h

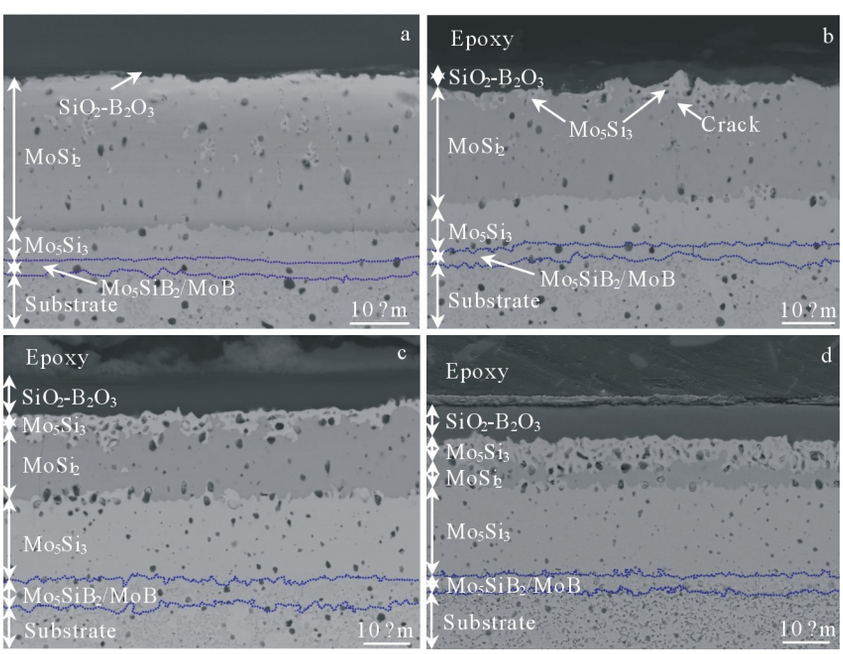

Fig.12 BSE images of cross-sectional coated bimodal (a~c) and FG (d) samples after oxidation at 1100 °C (a), 1200 °C (b) and 1300 °C (c, d) for 30 h

than the formation of MoO_3 at different temperatures. Additionally, the minimal oxygen partial pressure (P_{O_2}) required for reactions in Eq.(5) and Eq.(6) at 1100~1300 °C is calculated by Eq.(8)[26]:

$$\ln P_{O_2} = \frac{\Delta G}{2.303RT} \quad (8)$$

where R is the equilibrium gas constant. The P_{O_2} of reaction in Eq.(6) is lower than that of reaction in Eq.(5) at different temperatures. The fine MoB particles can supply B to form B_2O_3 (Eq. (7)), resulting in the development of SiO_2-B_2O_3 film[17]. The B_2O_3 can increase the fluidity of SiO_2 layer, promoting the sealing effect of pores in the outer layer[5]. At 1100~1300 °C, the MoO_3, Mo_5Si_3 and SiO_2-B_2O_3 form by reactions in Eq.(5~7) in the initial oxidation stage, respectively. The quick volatiliza-

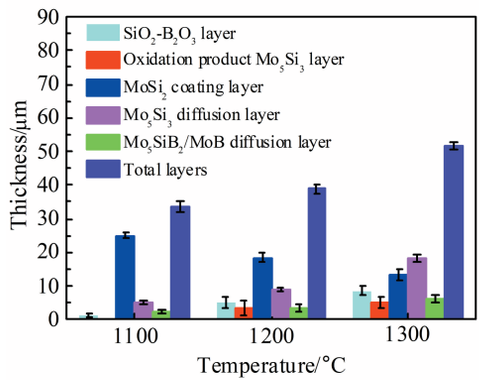

Fig.13 Thicknesses of different structural layers on substrate of coated bimodal specimens after oxidation at 1100~1300 °C

tion of MoO_3 causes the formation of porous scale and the transient mass loss of coating, which is consistent with the initial oxidation kinetics (Fig. 10). Meanwhile, the SiO_2-B_2O_3 grows, flows and develops a protective film on the $MoSi_2$ surface rapidly due to the high Si content in the coating. So the inward diffusion of oxygen is restricted and the oxygen partial pressure beneath the oxide scale decreases. When the oxidation process enters the middle and late stages, the SiO_2-B_2O_3 film thickens, and the oxygen partial pressure beneath the oxide scale is low, causing the selective oxidation of $MoSi_2$ coating[26]. The oxidation reaction with the lowest oxygen partial pressure is favored. Hence, the reaction in Eq.(6) is the dominant oxidation reaction producing the dominant product Mo_5Si_3[26].

At 1100 °C, the thickness of SiO_2-B_2O_3 film is very small and a few oxidation products Mo_5Si_3 form (Fig.12a), which indicates that the oxidation rate of the $MoSi_2$ is very low. At

Table 1 Gibbs free energy change Δ*G* and minimal oxygen partial pressure of reactions in Eq.(5) and Eq.(6) at different temperatures

Reaction	Temperature/°C	Gibbs free energy change, ΔG/kJ·mol^{-1}	Minimal oxygen partial pressure/Pa
Eq.(5)	1100	-743.828	5.08×10^{-29}
	1200	-738.811	6.38×10^{-27}
	1300	-733.923	4.29×10^{-25}
Eq.(6)	1100	-948.246	8.51×10^{-37}
	1200	-938.257	5.41×10^{-34}
	1300	-928.453	1.49×10^{-31}

1100 °C, the viscosity of SiO_2-B_2O_3 film is high. This high-viscosity film impedes the inward permeation of oxygen significantly. Thus, the reaction in Eq.(6) hardly proceeds. With increasing the temperature from 1100 °C to 1300 °C, the thickness of SiO_2-B_2O_3 film and layer of oxidation product Mo_5Si_3 increases gradually (Fig.13). Increasing temperature decreases the viscosity of SiO_2-B_2O_3 film, increasing the inward permeation rate of oxygen[5,17]. At 1200 and 1300 °C, when the real-time oxygen partial pressure beneath the oxide scale is higher than P_{O_2} required for reaction in Eq.(6), the reaction in Eq.(6) preferentially occurs. Compared to the situation at 1200 °C, the higher oxygen permeation rate accelerates the reaction in Eq.(6) at 1300 °C, resulting in the formation of more oxidation products. Because the oxidation products are not volatile, the oxidation behavior plots of coated bimodal alloys show the slight mass gain at 1200 and 1300 °C after 30 h (Fig.10). Besides, increasing the temperature promotes the flowing of SiO_2-B_2O_3 film, leading to the fact that outer scale becomes smooth (Fig.11). Moreover, the oxidation products Mo_5Si_3 of coated FG alloy are more than those of coated bimodal alloy at 1300 °C, indicating that the oxidation rate of unimodal $MoSi_2$ coating is higher than that of bimodal $MoSi_2$ coating. Compared to the bimodal $MoSi_2$ layer, the unimodal $MoSi_2$ layer has more grain boundaries, which increases the diffusion channels of oxygen and accelerates the reaction in Eq.(6)[27]. In addition, the La_2O_3 particles at the grain boundaries in the $MoSi_2$ layer reduce the transport rate of grain boundaries, which decreases the oxidation rate of $MoSi_2$[28].

The reaction diffusion paths in coating layers during oxidation process are illustrated in Fig.14. On the one hand, the oxidation of $MoSi_2$ coating consumes a small amount of Si, lead-

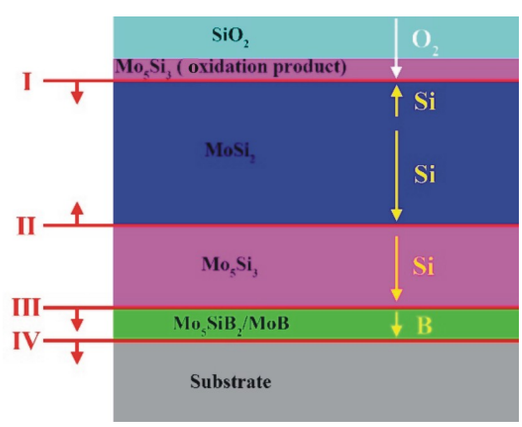

Fig.14 Schematic diagram of reaction diffusion paths in coating layers during oxidation process (red arrows indicate the growth direction of interfaces; yellow arrows indicate the diffusion direction of Si and B atoms; white arrow indicates the permeation direction of O_2)

ing to the downward movement of interface I. On the other hand, the in-diffusion behavior of Si from the $MoSi_2$ coating loses a large amount of Si. The $MoSi_2$ decomposes into Mo_5Si_3 and Si at the interface II, according to reaction in Eq.(9) as follows:

$$5MoSi_2 \rightarrow Mo_5Si_3+7Si \quad (9)$$

So the interface II moves upwards and the Si atoms diffuse through Mo_5Si_3 interlayer to interface III. The reactions in Eq.(10) and Eq.(11) at interface III contribute to the additional growth of Mo_5Si_3 and the interface III moves downwards.

$$2Si+Mo_5SiB_2 \rightarrow Mo_5Si_3B_x+(2-x)B \quad (10)$$

$$3Si+5MoB \rightarrow Mo_5Si_3B_x+(5-x)B \quad (11)$$

Because the solubility of B in the Mo_5Si_3 is very small, the additional B atoms diffuse toward the interface IV to promote the formation of Mo_5SiB_2/MoB. Thus, the movement of interface II and III results in the relatively rapid growth of Mo_5Si_3. With the calculation based on the thickness of layers (Fig.13), the growth rate of Mo_5Si_3 layer is always higher than that of Mo_5SiB_2/MoB layer at different temperatures. Moreover, with increasing the temperature, the thicknesses of Mo_5Si_3 and Mo_5SiB_2/MoB layers increase, and the thickness of $MoSi_2$ coating decreases, indicating that improving temperature accelerates the interdiffusion of Si and B. Continuous consumption of Si in the $MoSi_2$ for a long time during oxidation eventually causes the complete elimination of $MoSi_2$. Therefore, the content of B in the Mo_5Si_3 layer is saturated because the Mo_5Si_3 has close contact with the Mo_5SiB_2/MoB. The Mo_5Si_3 layer with B saturation usually shows good oxidation resistance above 1000 °C[29]. In addition, the Mo_5SiB_2/MoB-layer hinders the internal diffusion of Si because of the low self-diffusion coefficient of Si in the Mo_5SiB_2 and a negligible Si solubility in MoB[30,31]. Also, the Mo_5SiB_2 possesses excellent oxidation resistance[32]. Thus, the designed multilayered coatings can protect the bimodal substrate from oxidation consumption for a long time.

4 Conclusions

1) Developing a multilayered coating structure ($MoSi_2$, Mo_5Si_3 and Mo_5SiB_2/MoB) over the bimodal Mo-12Si-8.5B-0.57wt% La_2O_3 alloy via Si-pack cementation can significantly enhance its surface oxidation resistance at 1100~1300 °C and simultaneously maintain its superior mechanical properties.

2) Compared to the coating on the fine-grained substrate, the surface of coating on the bimodal substrate is rougher and exhibits bimodal microstructure. Besides, the La_2O_3 particles distributed in the coating toughens the coating.

3) The coated bimodal alloy exhibits a very small mass change after oxidation due to the quick formation of a thin and self-healing SiO_2-B_2O_3 protective film. As the temperature increases, the thickness of SiO_2-B_2O_3 film and the oxidation product Mo_5Si_3 increase since the viscosity of SiO_2-B_2O_3 film decreases. Also, raising temperature promotes the Si and B interdiffusion, increasing the thickness of Mo_5Si_3 and Mo_5SiB_2/MoB layers.

4) Compared to the coated bimodal alloy, the coated fine-grained alloy exhibits large oxidation mass gain at 1300 °C because the unimodal $MoSi_2$ coating has more grain boundaries.

References

1 Wen S H, Zhou C G, Sha J B. *Corrosion Science*[J], 2017, 127: 175

2 Makineni S K, Kini A R, Jägle E A *et al*. *Acta Materialia*[J], 2018, 151: 31

3 Choi W J, Park C W, Park J H *et al*. *International Journal of Refractory Metals and Hard Materials*[J], 2019, 81: 94

4 Li J F, Luo Z P. *Rare Metal Materials and Engineering*[J], 2020, 49(2): 712 (in Chinese)

5 Rioult F A, Imhoff S D, Sakidja R *et al*. *Acta Materialia*[J], 2009, 57(15): 4600

6 Wang J, Li B, Ren S *et al*. *Journal of Materials Science and Technology*[J], 2018, 34(3): 635

7 Krüger M, Franz S, Saage H *et al*. *Intermetallics*[J], 2008, 16(7): 933

8 Li R, Li B, Wang T *et al*. *Journal of Alloys and Compounds*[J], 2018, 743: 716

9 Wei X X, Jin L, Wang F H *et al*. *Journal of Materials Science and Technology*[J], 2020, 44: 19

10 Li R, Li B, Chen X *et al*. *Materials Science and Engineering A* [J], 2020, 772: 138 684

11 Das J, Roy B, Kumar N K *et al*. *Intermetallics*[J], 2017, 83: 101

12 Karahan T, Ouyang G Y, Ray P K *et al*. *Intermetallics*[J], 2017, 87: 38

13 Pang J, Wang W, Zhou C G. *Corrosion Science*[J], 2016, 105: 1

14 Sun J, Fu Q G, Guo L P *et al*. *Materials and Design*[J], 2016, 92: 602

15 Li B, Zhang G J, Lin X H *et al*. *Rare Metal Materials and Engineering*[J], 2018, 47(5): 1529 (in Chinese)

16 Wang Y, Wang D Z, Yan J H. *Journal of Alloys and Compounds* [J], 2014, 589: 384

17 Majumdar S. *Applied Surface Science*[J], 2017, 414: 18

18 Tang Z H, Thom A J, Kramer M J *et al*. *Intermetallics*[J], 2008, 16: 1125

19 Liu G, Zhang G J, Jiang F *et al*. *Nature Materials*[J], 2013, 12(4): 344

20 Chakraborty S P, Banerjee S, Sharma I G *et al*. *Journal of Nuclear Materials*[J], 2010, 403(1-3): 152

21 Sakidja R, Park J S, Hamann J *et al*. *Scripta Materialia*[J], 2005, 53(6): 723

22 Majumdar S, Sharma I, Samajdar I *et al*. *Journal of the Electrochemical Society*[J], 2008, 155(12): 734

23 Zhang H A, Wang D Z, Chen S P *et al*. *Materials Science and Engineering A*[J], 2003, 345(1-2): 118

24 Petrovic J J. *Intermetallics*[J], 2000, 8(9-11): 1175

25 Chen H, Ma Q, Shao X *et al*. *Materials Science and Engineering A*[J], 2014, 592: 12

26 Cai Z Y, Wu Y H, Liu H Y *et al*. *Materials and Design*[J], 2018,

155: 463
27 Liu Y Q, Shao G, Tsakiropoulos P. *Intermetallics*[J], 2001, 9: 125
28 Burk S, Gorr B, Trindade V B *et al*. *Corrosion Engineering, Science and Technology*[J], 2009, 44(3): 168
29 Perepezko J H, Sakidja R. *Advanced Engineering Materials*[J], 2009, 11(11): 892
30 Sakidja R, Perepezko J H, Kim S *et al*. *Acta Materialia*[J], 2008, 56(18): 5223
31 Kim S, Perepezko J H. *Journal of Phase Equilibria and Diffusion*[J], 2006, 27(6): 605
32 Yeh C L, Chen W L. *Vacuum*[J], 2019, 163: 288

双峰结构Mo-Si-B基体表面多层硅化物涂层的表征和抗氧化性能

李　瑞，陈　璇，王　娟，李　斌，王　涛，严富学，张国君
(西安理工大学 材料科学与工程学院，陕西 西安 710048)

摘　要：由于在细晶Mo-Si-B合金中制备双峰分布的α-Mo晶粒能够在不显著降低合金强度的前提下大幅提高其断裂韧性，为了加强双峰结构合金的表面防护，同时保持其优异的力学性能，通过包埋渗在合金表面上制备了一个具有多层结构（$MoSi_2$，Mo_5Si_3和Mo_5SiB_2/MoB）的涂层。研究结果表明，相比在细晶结构基体上制备的涂层，双峰结构基体上的涂层表面较为粗糙，并且也表现出双峰分布的微观组织。此外，覆盖涂层后的双峰结构合金的断裂韧性依然良好，并且分布在涂层中的La_2O_3颗粒能够增韧涂层。具有涂层的双峰结构合金在1100~1300 ℃下展现出了卓越的抗氧化性，这是由于氧化过程中在涂层表面快速形成了一个薄且能自愈合的SiO_2-B_2O_3膜。随着氧化温度升高，SiO_2-B_2O_3膜的粘度降低，使得SiO_2-B_2O_3膜的厚度和氧化产物Mo_5Si_3均增加。并且，升高温度促进了Si和B的互扩散，加速了Mo_5Si_3和Mo_5SiB_2/MoB层的增长。在1300 ℃下，由于单峰结构的$MoSi_2$涂层拥有更多的晶界，使得含涂层的细晶合金相比含涂层的双峰结构合金表现出更多的氧化增重。

关键词：$MoSi_2$涂层；Mo-12Si-8.5B合金；双峰结构的α-Mo晶粒；包埋渗；抗氧化性

作者简介：李　瑞，男，1988年生，博士生，西安理工大学材料科学与工程学院，陕西 西安 710048，电话：029-82312592，E-mail：maoruiruimail@sina.com